PNAS RESEARCH ARTICLE | APPLIED PHYSICAL SCIENCES

Dislocation-tuned ferroelectricity and ferromagnetism of the $BiFeO_3/SrRuO_3$ interface

Xiaomei Li[a,b,c,d,1], Bo Han[a,c,1], Ruixue Zhu[a,c,1], Ruochen Shi[a,c], Mei Wu[a,c], Yuanwei Sun[a,c], Yuehui Li[a,c], Bingyao Liu[a,c], Lifen Wang[d,e], Jingmin Zhang[c], Congbing Tan[f], Peng Gao[a,c,g,h,i,2], and Xuedong Bai[d,e,2]

Edited by Risto Nieminen, Aalto-yliopisto Teknillisen fysiikan laitos, Finland; received August 8, 2022; accepted February 5, 2023

Misfit dislocations at a heteroepitaxial interface produce huge strain and, thus, have a significant impact on the properties of the interface. Here, we use scanning transmission electron microscopy to demonstrate a quantitative unit-cell-by-unit-cell mapping of the lattice parameters and octahedral rotations around misfit dislocations at the $BiFeO_3/SrRuO_3$ interface. We find that huge strain field is achieved near dislocations, i.e., above 5% within the first three unit cells of the core, which is typically larger than that achieved from the regular epitaxy thin-film approach, thus significantly altering the magnitude and direction of the local ferroelectric dipole in $BiFeO_3$ and magnetic moments in $SrRuO_3$ near the interface. The strain field and, thus, the structural distortion can be further tuned by the dislocation type. Our atomic-scale study helps us to understand the effects of dislocations in this ferroelectricity/ferromagnetism heterostructure. Such defect engineering allows us to tune the local ferroelectric and ferromagnetic order parameters and the interface electromagnetic coupling, providing new opportunities to design nanosized electronic and spintronic devices.

misfit dislocations | ferroelectric | magnetic moments | atomic resolution | defect

Significance

In ferroelectric/ferromagnetic systems, misfit dislocations at the heteroepitaxial interface can significantly alter the local properties through strain-field–induced structural distortion. In this work, we use scanning transmission electron microscopy to unit-cell-by-unit-cell map the lattice parameters and octahedral rotations around misfit dislocations at the $BiFeO_3/SrRuO_3$ interface, and, thus, reveal the distinct effects of structural distortion on the local ferroelectricity and ferromagnetism properties. The results have important implications for interface engineering and device fabrication based on heteroepitaxial technology.

Perovskite oxide heterostructures, exhibiting exotic physical properties, such as the topological Hall effect (1), superconductivity (2, 3), and a two-dimensional electron gas (4), are attracting increasing attention due to the interfacial coupling involving lattice, charge, spin, and orbital order parameters. For multiferroic oxide heterojunctions in particular, the interactions between multiple ferroic orders at the interface make them promising candidates for high-performance electronic and spintronic devices (5). To tailor the properties of these oxide heterostructure, strain engineering, i.e., the use of epitaxy substrates with different lattice constant/symmetry to impose a strain to the thin film, is a very effective strategy. The underlying mechanism is that the lattice constant and oxygen octahedron distortion, which usually represents the electronic and magnetic properties of perovskite, are sensitive to the strain state. Thus, the properties can be dramatically tuned under different strain states. Although the state-of-the-art epitaxy growth has already achieved an order of magnitude higher than the critical strain value of crack in bulk, the typical level of imposed strain is limited at about +3% (6), above which the films usually tend to be relaxed with the formation of dislocation arrays at the interface, making a higher strain state still challenging to achieve.

In fact, dislocations in functional oxides are not always harmful; instead, they sometimes generate local fascinating properties that are unavailable in the bulk matrix. The reason is that they change the local atomic arrangement and introduce huge strain fields and gradients (7, 8) and even a different phase/composition, making the surrounding material exhibit unique properties that are different from the rest of the bulk. For example, in antiferromagnetic NiO crystals, the Ni deficiency at dislocation cores produces local ferromagnetic properties (9); in ferroelectric thin films, the strain field around dislocations can propagate in long distance, thus tuning the ferroelectric polarization (10, 11); in paraelectric $SrTiO_3$ (STO), the large strain gradients around dislocations generate ferroelectricity due to the flexoelectric effect (12). For prototype perovskite STO, a strain of up to 10% can be achieved within the first two unit cells of the dislocation core (12) and stays ~5%, extending over several nanometers (13, 14), which is typically larger than the value of regular epitaxy. Therefore, the misfit dislocations at the interface with huge strain and strain gradient can likely induce some exotic properties that are unavailable from ideal epitaxy growth.

In this work, we study the effects of misfit dislocation at the $BiFeO_3/SrRuO_3$ (BFO/SRO) interface with the aim of obtaining new strategies to tune the interfacial electronic and magnetic properties. Recent studies reveal some exotic phenomena in the BFO/SRO multiferroic heterojunctions, such as the topological Hall effect that is induced by the Dzyaloshinskii–Moriya interaction (DMI) through magnetoelectric coupling at the interface

Author contributions: P.G. and X.B. designed research; X.L., B.H., R.Z., Y.S., and C.T. performed research; R.S., M.W., L.W., and J.Z. contributed new reagents/analytic tools; X.L., Y.L., and B.L. analyzed data; and X.L., R.Z., and P.G. wrote the paper.

The authors declare no competing interest.

This article is a PNAS Direct Submission.

[1]X.L., B.H., and R.Z. contributed equally to this work.

[2]To whom correspondence may be addressed. Email: p-gao@pku.edu.cn or xdbai@iphy.ac.cn.

This article contains supporting information online at https://www.pnas.org/lookup/suppl/doi:10.1073/pnas.2213650120/-/DCSupplemental.

Published March 20, 2023.

(15). The properties of both BFO and SRO are sensitive to the strain state; thus, a variety of parameters can have a significant impact on the electronic structure and magnetic properties and further affect the coupling between BFO and SRO at the interface, including epitaxial strain (16–19), film thickness variation (20–22), reversal of ferroelectric polarization (23, 24), and variation of the rotation angle of the oxygen octahedron (25–27).

We use advanced scanning transmission electron microscopy (STEM) imaging and spectroscopy to reveal a direct, quantitative unit-cell-by-unit-cell mapping of lattice parameters and oxygen octahedral rotation around the misfit dislocation at the epitaxial BFO/SRO interface, allowing us to directly correlate the atomic structure and chemistry of the misfit dislocation core with its surrounding strain field, the polarization of BFO, and the ferromagnetism of SRO on the atomic level. We find that interfacial dislocation induces a huge local strain field of more than 5%, but the impact on BFO and SRO is different, i.e., BFO is subjected to tensile strain, resulting in a main change in the lattice distortion for about 8 unit cell., while SRO is subjected to compressive strain, resulting in a significant decrease in the oxygen octahedron rotation for about 8 u.c. As a result, near the dislocation, both the ferroelectric polarization in BFO and magnetic moments in SRO are changed at the interface, which further alters the magnetoelectric coupling behavior at the interface. These atomic-scale findings provide insights into understanding the effects of dislocations in such a ferroelectricity and ferromagnetism heterostructure system. Furthermore, the dislocation enables a locally huge strain field that is unavailable from regular substrate strain engineering, suggesting a new strategy to design electronic, ferroelectric, magnetic, and magnetoelectric functions via proper defect engineering.

Results

Atomic Structure of Misfit Dislocation Core. Fig. 1*A* is a high-angle annular dark-field (HAADF)-STEM image, acquired along the [001] zone-axis for multiferroic BFO grown on an STO $(110)_c$ substrate, with a ferromagnetic SRO buffer layer. Due to the large lattice mismatch of STO and BFO in the in-plane direction (parallel to the interface), misfit dislocation arrays with burgers vector $\mathbf{b} = \sqrt{2}\mathbf{a}[1\bar{1}0]$ (in Fig. 1*A* and enlarged view in Fig. 1*B*) appear at the SRO/BFO interface. The atomic number–sensitive HAADF image and atomically resolved EDS maps in Fig. 1 *C*–*H* show that Bi atoms diffuse into the dislocation core in a triangular shape. The elemental changes are quantitively plotted in Fig. 1*I* and *SI Appendix*, Fig. S1, showing an enrichment of Bi and a deficiency of Sr at the dislocation core when compared with the normal interface. The excess Bi atoms seem to not only occupy the A site but also the B site in the dislocation core, forming a tiny Bi_2O_3 cluster between a pair of partial dislocations (*SI Appendix*, Fig. S2), which has also been observed in BFO thin films (7, 28, 29). In our case, the relatively large atomic radius of the enriched Bi element accumulating at the dislocation core would be helpful for the strain accommodation (8). As shown in Fig. 1*J*, the Fe-L_3 edge at the misfit dislocation core is slightly shifted to lower energies, and the intensity of the L_2 edge at the dislocation core is slightly higher than that of the bulk, which qualitatively confirms a drop in the Fe valence state around the misfit dislocation core (30, 31). The intensity of O peaks at the dislocation core is obviously reduced, as shown in Fig. 1*K*, implying the existence of oxygen vacancies (32), which may be able to stabilize the electrical neutrality condition and accommodate the strain through the chemical expansion (33).

To explore the effect of strain on the BFO/SRO interface, we measured the lattice constant and oxygen octahedral distortion

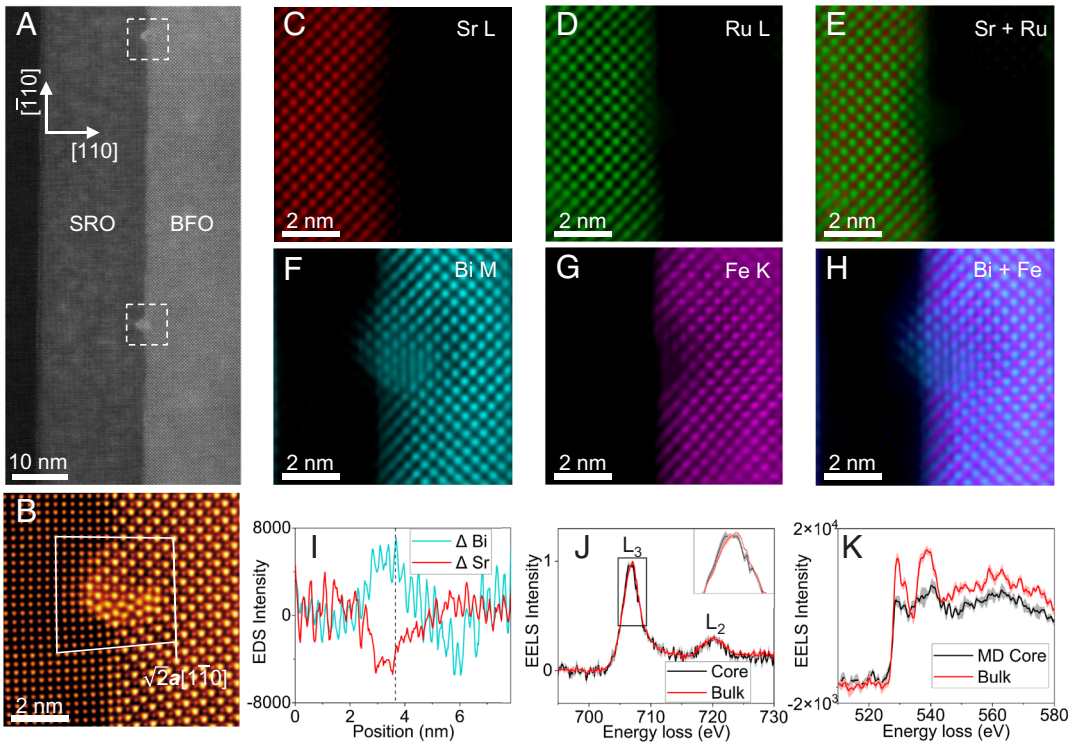

Fig. 1. Atomic structure of the misfit dislocation core. (*A*) A HAADF-STEM image showing two misfit dislocations at the interface, as shown in the white dotted box. (*B*) High-magnification HAADF image showing the atomic structure of the misfit dislocation core and Burgers vector: $\sqrt{2}a[1\bar{1}0]$. Atomically resolved EDS mapping determining the cationic configuration in the misfit dislocation core corresponding to *B*: (*C*) Sr, (*D*) Ru, (*E*) Sr + Ru, (*F*) Bi, (*G*) Fe, (*H*) Bi+Fe. (*I*) Differences between Sr and Bi elements with line profiles across the dislocation core and defect-free interface. (*J*) Fe-*L* edges and (*K*) O-*K* edges from the misfit dislocation core (black) and bulk (red). The *Inset* of *J* is a local enlarged view of the Fe-L_3 peak.

around the misfit dislocation. Based on the position of Bi and Fe atoms from the HAADF image (Fig. 2*A*), as illustrated in Fig. 2*B*, we define d_{12} and d_{14} to represent the lattice constants in the [010] and [100] directions, respectively. θ_1 is the angle between d_{14} and the horizontal direction, which is used to reflect the rotation of the entire unit cell. The unit-cell–wise d_{14}/d_{12} mapping in Fig. 2*C* shows a significant variation along the interface, where d_{14}/d_{12} increases substantially in the upper region of the dislocation (change up to ~13%, red line profile I in Fig. 2*E* corresponding to the red rectangle region in Fig. 2*C*) and decreases in the bottom region (change up to ~8%, blue line profile II corresponding to the blue rectangle region in Fig. 2*C*). Notably, lattice distortion away from the dislocation is insignificant (black line profile III). The inset of Fig. 2*E* schematically displays the lattice distortion in different regions, supported by the individual changes of d_{12} and d_{14} shown in *SI Appendix*, Fig. S3. Another effect of misfit dislocation on the distortion of the surrounding lattice is the variation of θ_1 (change over ~6%, Fig. 2*D* and the corresponding line profiles in Fig. 2*F*). As schematically shown in Fig. 2*F*, the direction of the lattice rotation on the upper and lower sides of the dislocation is opposite. However, the bond angle between d_{14} and d_{12} is weakly affected by the dislocation (*SI Appendix*, Fig. S3*D*). It is also worth noting that the lattice distortion in BFO, including changes in the lattice constant and lattice rotation angle, is more significant than that of SRO.

To investigate the effect of misfit dislocations on the oxygen octahedron rotation angle, we performed integrated differential phase contrast (iDPC) imaging (*SI Appendix*, Fig. S4*A* and an enlarged view in Fig. 2*G*), which enables the simultaneous imaging of both cations and oxygen (34). Consistent with previous reports (18), here, we use the rotation angle $\alpha = (90° - \Omega)/2$ to reflect the change of the rotation angle of the oxygen octahedron, where Ω is the angle among three oxygen ions between two corner-shared oxygen octahedra in the *x*–*y* plane, as shown in Fig. 2*G*. It is worth noting that the four nearest neighbors at the same position as Ω shown in Fig. 2*G* are the bond angles of the oxygen octahedron.

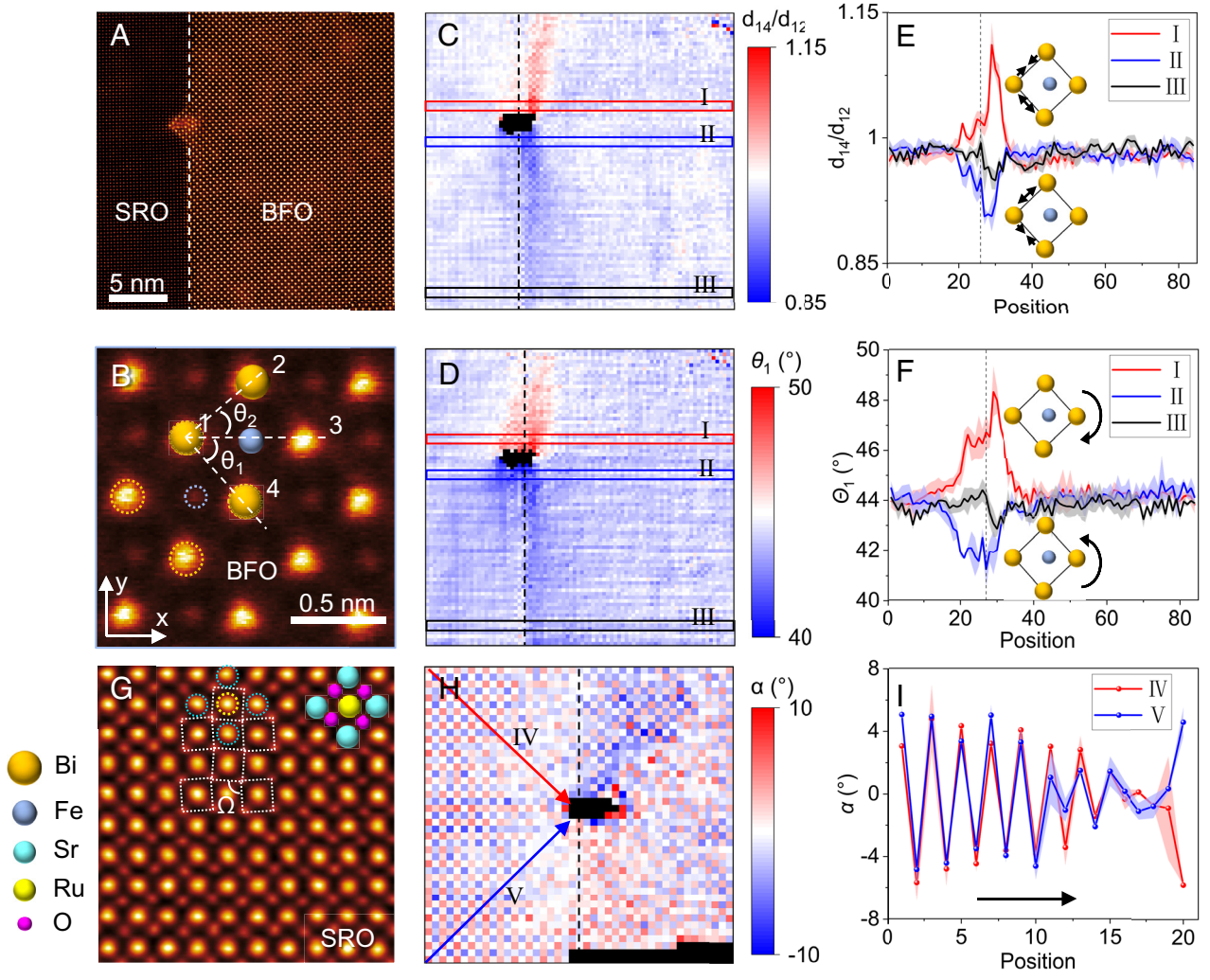

Fig. 2. Dislocation-induced structural distortion. (*A*) HAADF image of the interface (highlighted by the white line). (*B*) Digitally magnified HAADF image from the BFO region showing atomic and angle definitions. (*C* and *D*) Distribution of *C* lattice constant ratios (d_{14}/d_{12}, as defined in *B*) and *D* lattice rotation (θ_1, as defined in *B*) corresponding to the HAADF image in *A*. The black dotted lines mark the interface. Black spots are missing values due to huge structure changes at the dislocation core. (*E*) Horizontal lattice constant ratios line profiles corresponding to *C*. Line profiles I, II, and III correspond to the distribution of d_{14}/d_{12} along the red, blue, and black rectangle regions in *C*, respectively. The schematic depicts the change in the lattice constant in both directions. (*F*) Horizontal lattice rotation line profiles corresponding to *D*. Line profiles I, II, and III correspond to the distribution of θ_1(°) along the red, blue, and black rectangle regions in *D*, respectively. The schematic displays the rotation direction of the lattice in the vicinity of the misfit dislocation. (*G*) Digitally magnified iDPC image of SRO (from the blue box in *SI Appendix*, Fig. S3*A*); Sr, Ru, and O are visible at the same time and the white dotted outlines mark the oxygen octahedrons. (*H*) Variation of the rotation angle (α, $\alpha = (90° - \Omega)/2$) of the oxygen octahedron. (*I*) Line profiles of oxygen octahedron rotation angles corresponding to the red (IV) and blue (V) lines in *H*. Error bars (shade color) are the SDs calculated used three sets of data (pixels) in the vicinity of the line.

The unit-cell-scale mapping of α in Fig. 2*H* and the distribution of α along the red (IV) and blue (V) line profiles in Fig. 2*I* show that the presence of the misfit dislocation significantly reduces the oxygen octahedron rotation angle of the nearby SRO. As for BFO, the rotation direction of the oxygen octahedron is opposite along this observation direction, so the corresponding behavior of the oxygen octahedron cannot be analyzed well (*SI Appendix*, Fig. S4*B*). In particular, even though the rotation angles of RuO_6 oxygen octahedra decrease from ~5° in bulk to ~0.5° near the dislocation, as shown in Fig. 2*I*, their bond angles exhibit no obvious change (*SI Appendix*, Fig. S4*C*), i.e., the effect of compressive strain on SRO is mainly reflected in the change of oxygen octahedral rotation rather than the change of the whole unit cell.

These structural modifications significantly affect the local properties. Considering that the spontaneous polarization in BFO has a linear relationship with the displacement of cations relative to the surrounding cation centers (*SI Appendix*, S5) (35–37), the magnitude of polar atomic displacement vector $-\boldsymbol{D}_{FB}$ is used to represent the polarization magnitude. The influence of the misfit dislocation on the surrounding polar atomic displacement is shown in Fig. 3*A*, where the presence of the misfit dislocation leads to a decrease in the polarization magnitude and a rotation of the polarization direction near the defect. Fig. 3*B* shows the full-area displacement magnitude distribution corresponding to Fig. 2*A*; the black dotted line shows the location of the interface in the HAADF image. The polar atomic displacement of BFO is reduced at the interface and such a reduction is more significant around the dislocation core, while the displacement also appears on the SRO side near the interface. The slight fluctuations in the displacement between different regions (e.g., the top part and bottom in Fig. 3*B*) may be caused by the tiny mistilt of bending specimen (38). This can also be reflected in the horizontal distribution of the displacement magnitude along the red frame (I), blue frame (II), and black frame (III) in Fig. 3*B*, as shown in Fig. 3*C*. For the position away from the dislocation (III, approximate bulk), the existence of the interface affects the out-of-plane displacement in the range of ~3 u.c. in BFO and ~1 u.c. in SRO due to the screening mechanism. However, at the interface with dislocation, such an effect is dramatically changed. For the periphery of the defect (I and II), the displacement in BFO is changed (suppressed D_x along out-of-plane and enhanced D_y along in-plane) within ~9 u.c. away near the interface (*SI Appendix*, Fig. S6), while in SRO, the change of displacement occurs at a distance of 4 u.c. within the interface. This demonstrates a reduction (increase) in the polarization of BFO (SRO) spanning a range of about 6 (4) u.c. in the out-of-plane direction (perpendicular to the interface) and about 30 u.c. in the in-plane direction (along the interface direction). This is in good agreement with the range of lattice distortions shown in Fig. 2. Moreover, Fig. 3*D* shows the atomic structure of the misfit dislocation core viewed from the [$\bar{1}$10] axis (the locally enlarged view corresponding to the white box in *SI Appendix*, Fig. S7). The segregation and enrichment of Bi element also exist at the dislocation core, which can be reflected from the Z-contrast HAADF image. The middle Fe atoms around the dislocation core seem to have a large offset relative to the center of Bi atoms, which is further confirmed by the displacement mapping (red region in Fig. 3*E*) and the horizontal distribution of the red frame (I), blue frame (II), and black frame (III) in Fig. 3*F*. It is noteworthy that the displacement is only enhanced above the dislocation core (promotes the transition from the R phase to the T-like phase), while there is no significant change along the interface.

Furthermore, the electronic structure and magnetic properties of SRO, which can be easily affected by the hybridization between Ru-*d* orbitals and O-*p* orbitals through manipulating the rotations of octahedra (26, 39, 40), also become different near the dislocation. In order to evaluate the effect of the suppressed rotation of the oxygen octahedrons at SRO around dislocations, we performed first-principles calculations. Fig. 4*A* shows the optimized atomic structure of bulk SRO and the reduced rotation angle SRO, respectively. Consistent with experimental observations, the rotation angle of the oxygen octahedron is reduced to ~0.5° in the modeling. The reference value in the bulk is ~5°. From Fig. 4*B*, the electron pocket above the Fermi level reduces its energy and even passes through the Fermi level as the rotation angle of the oxygen octahedron decreases, modifying the density of states (DOS) near the Fermi level, which may alter the electronic and transportation properties of SRO. Regarding magnetic properties, the calculated Ru magnetic moment for bulk SRO is 1.36 μ_B/Ru, which is in good agreement

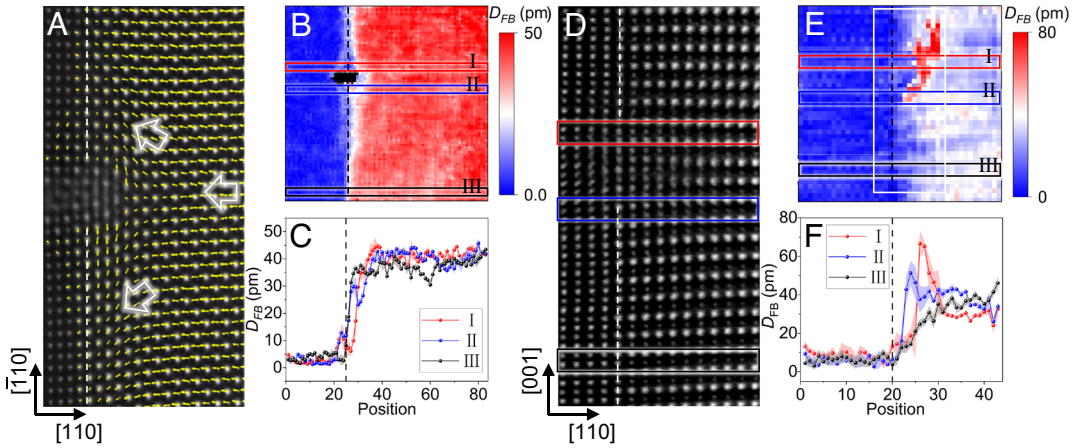

Fig. 3. Influences of structural distortion on BFO ferroelectric polarization. (*A*) Enlarged view of the HAADF image in Fig. 2*A* overlaid with polar vectors (the magnitude is proportional to the cation displacement, and the direction is opposite to the cation displacement) showing the variation of BFO polarization near the misfit dislocation core. White arrows denote the polarization direction of BFO. Due to the presence of misfit dislocations, the direction and magnitude of the surrounding polarization change. (*B*) Polar atomic displacement magnitude mapping of the central cation relative to the four surrounding cations corresponding to the image in Fig. 2*A*, showing the decrease in polarization around the misfit dislocation. The black dotted lines mark the interface. Black spots are missing values due to huge structure changes at the dislocation core. (*C*) Horizontal distribution of polar atomic displacement magnitude along the red frame (I), blue frame (II), and black frame (III) in *B*, showing the decrease in polarization magnitude induced by the misfit dislocation. (*D*) HAADF image of the misfit dislocation core viewed from the [$\bar{1}$10] axis. (*E*) Mapping of the displacement of the central cation relative to the centers of the two cations above and below it. The white box corresponds to the region shown in *D*. (*F*) Displacement magnitude line profiles extracted from the region above (red), below (blue), and ~8 u.c. away from the dislocation (black), showing the increase in polarization above the misfit dislocation and decrease beside the misfit dislocation.

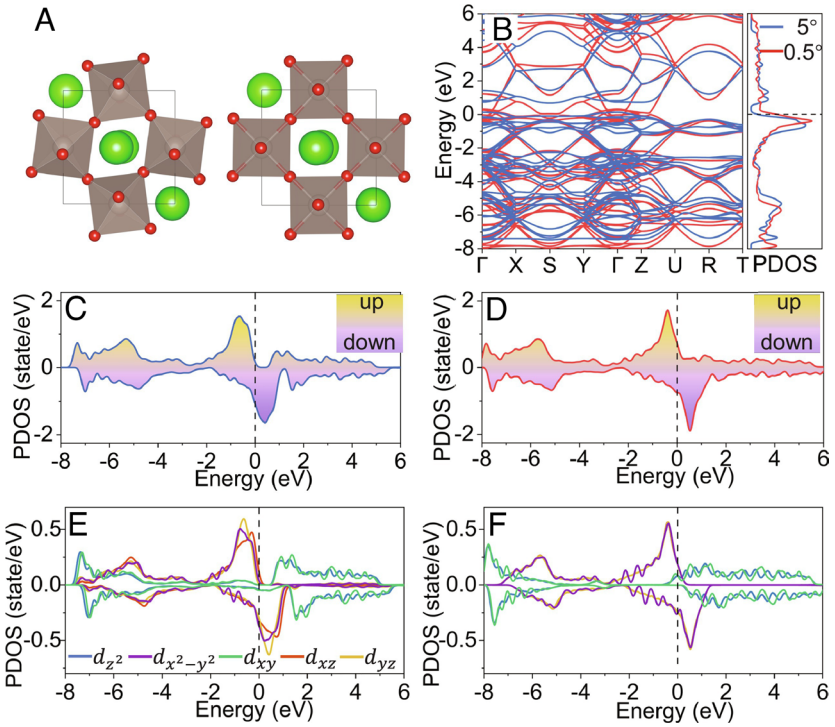

Fig. 4. Influences of structural distortion on SRO electronic structure and magnetism. (*A*) Optimized atomic structure of bulk SRO (*Left*) and reduced rotation angle SRO (*Right*). (*B*) Band structures of bulk and SRO with reduced rotation angle. Ru-site–projected partial DOS of (*C*) bulk SRO and (*D*) SRO with reduced rotation angle. Orbital-resolved DOS of Ru atoms for (*E*) bulk and (*F*) reduced rotation angle SRO.

with previous results (26, 41). The decrease in the rotation angle of the oxygen octahedron reduces the magnetic moment to 1.21 μ_B/Ru. Considering the magnetism of SRO mainly originates from the contribution of Ru atoms, Fig. 4 *C* and *D* show the projected DOS of the two spin channels corresponding to a Ru atom in bulk and in the reduced rotation model, respectively. With the suppression of the rotation angle, the DOS of two spin channels becomes more symmetrical, indicating the reduction of magnetic moments. The orbital-resolved DOS on the Ru atom in Fig. 4 *E* and *F* shows that the oxygen octahedron rotation suppression induces the redistribution of the *d* orbital near the Fermi level. Changes in the number of electron occupancies for the two spin states of each orbital below the Fermi level were also calculated, as shown in *SI Appendix*, Table S1. Comparing Fig. 4 *E* and *F*, the most obvious change in electronic states is that the projected DOS of d_{z^2} and d_{xy} orbitals prefers to fill the lower part of the energy region above the Fermi level. The reduction in magnetic moment, mainly attributed to the change of d_{yz}, d_{xz} and $d_{x^2-y^2}$, results from the decreased rotation angle, as detailed in *SI Appendix*, Table S1. This result suggests that the orbital reconstruction caused by structural distortions will affect the electrical and magnetic properties of the SRO. In addition, the DOS at the Fermi level changes with the reduction of the tilt angle, indicating the change of T_c values (22), and the variation in orbitals will also induce the change in magnetic anisotropy (42, 43).

Discussion

Interfacial dislocation–induced strain has different impacts on the BFO and SRO, as identified in the above atomic-scale analysis. The multiferroic BFO is subjected to tensile strain, mainly resulting in the change of lattice constants and lattice rotation, accompanied by nearby symmetry breaking and ferroelectric polarization suppression and rotation. Ferromagnetic SRO, on the other hand, subjected to compressive strain, results in a decrease in the tilt angle of the oxygen octahedron. It is worth noting that the influence of misfit dislocations on the BFO side decays very quickly in the direction perpendicular to the interface (~6 u.c.) but propagates far along the interface (~30 u.c.). This difference likely depends on the Burgers vectors of misfit dislocations. As shown in *SI Appendix*, Fig. S8, the effect of two adjacent half-dislocations on lattice distortion is quite different from that of full dislocations introduced above, that is, the influence of two adjacent half-dislocations on the lattice distortion is no longer along the interface direction, but mainly concentrated in the out-of-plane direction. The strain field induced by interfacial misfit dislocations is concentrated along specific directions relative to the Burgers vector rather than a radial distribution, which is inconsistent with previous reports (8). Therefore, by controlling the type and Burgers vectors of misfit dislocations via defect engineering, the local strain field distribution can be controlled, and the related properties of functional materials can be tuned at the atomic scale.

Furthermore, the dislocation at BFO/SRO interface should change the electrical activity and the ferroelectric–magnetic coupling, which help us to understand its effects in devices and may further guide us to tune the properties of electronic, ferroelectric, and spintronic devices. For the electronic and ferroelectric devices, aggregation of oxygen vacancies and Bi segregation at the core of the interfacial misfit dislocation array lead to the change of electrical activity (44), the polarization homogeneity (Fig. 3 *B* and *E*), screening mechanism for ferroelectric polarization, and ferroelectric switching kinetics (e.g., due to the changed nucleation barrier and dislocation pinning to domain wall motion). Cooperating with the polarization bound charge, Schottky barrier height at the interface and thus depletion layer also change. For example, in the case of downward polarization in this work, the larger Schottky barrier–induced wider depletion layer should enhance the photovoltaic effect (45), change the leakage current (46), and affect the electrical transport properties in many ways. For the ferroelectric–magnetic coupling, due to the ferroelectric proximity effect, the space inversion symmetry in the SRO near the interface is broken

(the Ru atoms deviate from the Sr atom center to generate the atomic displacement, as shown in Figs. 3 *B* and *C*), triggering the sizeable interface DMI (47–49), which is further expected to make the magnetic skyrmions appear in SRO. The presence of dislocations likely alters the interface DMI based on its Hamiltonian ($H_{\mathrm{DMI}} = \mathbf{D}_{12} \cdot (\mathbf{S}_1 \times \mathbf{S}_2)$) (47), where $\mathbf{D}_{12}$ is the DMI vector. Since the displacement of SRO is more significant near the dislocation cores in Fig. 3 *B* and *C*, the $\mathbf{D}_{12}$ should be enhanced. So, although both ferroelectricity of BFO and ferromagnetism of SRO are suppressed around the dislocation core, the total DMI doesn't have to be reduced due to the enhancement of $\mathbf{D}_{12}$. Note that the dislocation density at the interface can be tuned through substrate strain engineering, enabling the tunable distribution of strain field at the interface, which further tunes the skyrmions (47–49) such as size and ordering.

Nevertheless, we would like not to emphasize the "enhancement" of property in this work. Instead, our intention is to emphasize the "tunable" properties with the presence of dislocations. For example, besides those properties related with electrical activity mentioned above, the atomic-size dislocation can cause nanoscale inhomogeneous ferroelectric–magnetic coupling, which is expected to change the local property such as magnetic skyrmions. Considering the one-dimensional dislocation "tubes" are arrays aligned along the interface, of which the presence is expected to generate considerable effects to the global interface properties. Furthermore, such dislocation effects depend on the dislocation type (i.e., dislocations with Burgers vectors $\boldsymbol{a}[0\bar{1}0]$ have different influences on the lattice structure as shown in *SI Appendix*, Fig. S8). Also note that the interface dislocations such as their density can be controlled by the substrate strain in some degree. All of these suggest that both of the local and global interface properties can be tuned by introducing the dislocations, which provide us new opportunities to design new types of electronic, ferroelectric, and spintronic devices.

Conclusion

We combined atomic-scale quantitative measurements and first-principles calculations to investigate the effect of the misfit dislocation at the BFO/SRO multiferroic heterojunction interface on the local structure and properties. At the core of the misfit dislocation, the segregation of Bi elements (Bi substitution in the Fe sites), the generation of oxygen vacancies, and the reduction of Fe valence accommodate large local strain. Around the dislocations, the lattice constants of the surrounding BFO significantly change (lattice constant ratio changes up to 10% and lattice rotation angle changes over 6%), leading to the suppression and rotation of the ferroelectric dipoles near the interface. Meanwhile, the tilt angle of the oxygen octahedron of SRO decreases from ~5° to ~0.5°, which affects the spin-orbital coupling and, thus, reduces the magnetic moment. Such a change will inevitably alter the magnetoelectric coupling at the interface of the multiferroic heterojunction and, thus, the performance of the electronic device composed of it. This work provides atomic-scale insights into understanding the effects of dislocations on ferroelectric and ferromagnetic properties in complex oxides and also a new strategy of defect engineering to achieve wide-range tuning of magnetoelectric functions in oxide heterostructures.

Materials and Methods

Film Deposition Details. BFO film was deposited on a (110)-STO substrate with an SRO-buffered layer in a pulsed laser deposition system (PVD-5000) equipped with a KrF excimer laser (λ = 248 nm). Ceramic targets of SRO and BFO (1 mol% Bi-enriched) were used for SRO and BFO layer deposition. SRO was first grown at 690 °C and 80-mTorr oxygen pressure, and then, the oxygen pressure was raised to 100-mTorr for the deposition of the BFO film. By controlling the growth time, the thicknesses of the SRO and BFO layers were ~18 nm and ~86 nm, respectively. Immediately after growth, the BFO/SRO heterostructure films were annealed at 690 °C for 10 min and then cooled down to room temperature.

Preparation of TEM Samples. The TEM specimens were first thinned by mechanical polishing and then subjected to argon ion milling. The ion-milling process was carried out using a Precision Ion Polishing System (PIPS)™ (Model 695, Gatan, Inc.) with an accelerating voltage of 3.0 kV until a hole was observed. Low-voltage milling was performed with an accelerating voltage of 0.5 kV to remove the surface amorphous layer and minimize the irradiation-damaged layers.

Electron Microscopy Characterization and Image Analysis. HAADF and iDPC images were recorded at 300 kV using aberration-corrected JEOL ARM 300F and FEI Titan Themis G2 microscopes. The convergence semiangle for imaging was 30 mrad, and the collection semiangle snap range was 4 to 21 mrad for iDPC imaging and 50 to 200 mrad for HAADF imaging. To obtain a sufficient signal-to-noise ratio for quantitative analysis, the iDPC image was acquired at 4,096 × 4,096 pixels, with a dwell time of 500 ms/pixel and a beam current of 20 pA to avoid beam damage. STEM-EELS spectra were recorded using a Nion HERMES 200 microscope. To reduce beam damage, EELS experiments were performed at 60 kV. The probe convergence semiangle was 35 mrad, and the collection semiangle was in the range of 24.9 mrad.

Polarization Mapping. The position of each atom in the HAADF and iDPC images was determined by simultaneously fitting with a 2D Gaussian peak to an a priori perovskite unit cell using a MATLAB code. The polarization distribution was then obtained.

First-Principles Calculations. The first-principles calculations were performed within Quantum ESPRESSO using the projector augmented wave pseudopotential Perdew–Burke–Enzerhof exchange-correlation functional. The atomic positions of SRO were optimized under an orthorhombic symmetry (with optimized cell parameters a = 5.591 Å, b = 5.573 Å, c = 7.885 Å). For self-consistent field calculations, the charge cutoff energy was 600 eV and the wavefunction cutoff was 60 eV. The DOS was calculated by interpolating the dynamic matrix on an 8 × 8 × 8 momentum mesh.

Data, Materials, and Software Availability. All data, materials, and experimental procedures that support the findings of this study are available in the text, *Methods*, and *SI Appendix*. The raw data of the TEM images involved in this article have been deposited at https://osf.io/qz5ak/ (50).

ACKNOWLEDGMENTS. This research was supported by the National Key R&D Program of China [2021YFA1400204 (X.B.)], National Natural Science Foundation of China [12104017 (X.L.), 52125307 (P.G.), 51991344 (X.B.), 52021006 (P.G.), T2188101 (P.G.)], the Chinese Academy of Sciences [XDB33030200 (X.B.), ZDYZ2015-1 (X.B.)], and "2011 Program" Peking-Tsinghua-IOP Collaborative Innovation Center of Quantum Matter, and open research fund of Songshan Lake Materials Laboratory [2022SLABFK03 (P.G.), 2021SLABFN14 (C.T.)], the Hunan Provincial Natural Science Foundation of China [2021JJ30234 (C.T.)], the Scientific Research Fund of Hunan Provincial Education Department [21A0311 (C.T.)], and the Guangdong Provincial Key Laboratory Program [Grant No. 2021B 1212040001 (C.T.)]. We are grateful for the computational resources provided by the High-Performance Computing Platform of Peking University.

Author affiliations: [a]International Center for Quantum Materials, School of Physics, Peking University, Beijing 100871, China; [b]School of Integrated Circuits, East China Normal University, Shanghai 200241, China; [c]Electron Microscopy Laboratory, School of Physics, Peking University, Beijing 100871, China; [d]Beijing National Laboratory for Condensed Matter Physics and Institute of Physics, Chinese Academy of Sciences, Beijing 100190, China; [e]School of Physical Sciences, University of Chinese Academy of Sciences, Beijing 100049, China; [f]Hunan Provincial Key Laboratory of Intelligent Sensors and Advanced Sensor Materials, School of Physics and Electronics, Hunan University of Science and Technology, Xiangtan 411201, China; [g]Frontiers Science Center for Nano-optoelectronics, School of Physics, Peking University, Beijing 100871, China; [h]Interdisciplinary Institute of Light-Element Quantum Materials and Research Center for Light-Element Advanced Materials, Peking University, Beijing 100871, China; and [i]Hefei National Laboratory, Hefei 230088, China

1. J. Matsuno *et al.*, Interface-driven topological Hall effect in $SrRuO_3$-$SrIrO_3$ bilayer. *Sci. Adv.* **2**, 1600304 (2016).
2. J. P. Ruf *et al.*, Strain-stabilized superconductivity. *Nat. Commun.* **12**, 59 (2021).
3. K. Ahadi *et al.*, Enhancing superconductivity in $SrTiO_3$ films with strain. *Sci. Adv.* **5**, eaaw0120 (2019).
4. S. Thiel, G. Hammerl, A. Schmehl, C. W. Schneider, J. Mannhart, Tunable quasi-two-dimensional electron gases in oxide heterostructures. *Science* **313**, 1942–1945 (2006).
5. H. Y. Hwang *et al.*, Emergent phenomena at oxide interfaces. *Nat. Mater* **11**, 103–113 (2012).
6. D. G. Schlom *et al.*, Elastic strain engineering of ferroic oxides. *MRS Bull.* **39**, 118–130 (2014).
7. M. Arredondo *et al.*, Direct evidence for cation non-stoichiometry and cottrell atmospheres around dislocation cores in functional oxide interfaces. *Adv. Mater.* **22**, 2430–2434 (2010).
8. C. P. Chang *et al.*, Condensation of two-dimensional oxide-interfacial charges into one-dimensional electron chains by the misfit-dislocation strain field. *Nat. Commun.* **5**, 3522 (2014).
9. I. Sugiyama *et al.*, Ferromagnetic dislocations in antiferromagnetic NiO. *Nat. Nanotechnol.* **8**, 266–270 (2013).
10. C. L. Jia *et al.*, Effect of a single dislocation in a heterostructure layer on the local polarization of a ferroelectric layer. *Phys. Rev. Lett.* **102**, 117601 (2009).
11. Y. L. Tang, Y. L. Zhu, Y. Liu, Y. J. Wang, X. L. Ma, Giant linear strain gradient with extremely low elastic energy in a perovskite nanostructure array. *Nat. Commun.* **8**, 15994 (2017).
12. P. Gao *et al.*, Atomic-scale measurement of flexoelectric polarization at $SrTiO_3$ dislocations. *Phys. Rev. Lett.* **120**, 267601 (2018).
13. M. W. Chu *et al.*, Impact of misfit dislocations on the polarization instability of epitaxial nanostructured ferroelectric perovskites. *Nat. Mater.* **3**, 87–90 (2004).
14. V. Nagarajan *et al.*, Misfit dislocations in nanoscale ferroelectric heterostructures. *Appl. Phy. Lett.* **86**, 192910 (2005).
15. H. Wang *et al.*, Overcoming the limits of the interfacial Dzyaloshinskii-Moriya interaction by antiferromagnetic order in multiferroic heterostructures. *Adv. Mater.* **32**, 1904415 (2020).
16. W. L. Lu *et al.*, Strain engineering of octahedral rotations and physical properties of $SrRuO_3$ films. *Sci. Rep.* **5**, 10245 (2015).
17. A. T. Zayak, X. Huang, J. B. Neaton, K. M. Rabe, Manipulating magnetic properties of SrRuO3 and CaRuO3 with epitaxial and uniaxial strains. *Phys. Rev. B* **77**, 214410 (2008).
18. A. T. Zayak, X. Huang, J. B. Neaton, K. M. Rabe, Structural, electronic, and magnetic properties of SrRuO3 under epitaxial strain. *Phys. Rev. B* **74**, 094104 (2006).
19. C. U. Jung, H. Yamada, M. Kawasaki, Y. Tokura, Magnetic anisotropy control of SrRuO3 films by tunable epitaxial strain. *Appl. Phy. Lett.* **84**, 2590–2592 (2004).
20. S. G. Jeong *et al.*, Propagation control of octahedral tilt in SrRuO3 via artificial heterostructuring. *Adv. Sci.* **7**, 2001643 (2020).
21. X. Shen *et al.*, Thickness-dependent metal-insulator transition in epitaxial SrRuO3 ultrathin films. *J. Appl. Phys.* **117**, 015307 (2015).
22. Y. J. Chang *et al.*, Fundamental thickness limit of itinerant ferromagnetic $SrRuO_3$ thin films. *Phys. Rev. Lett.* **103**, 057201 (2009).
23. S. Yan, Z. Li, D. Wang, W. Mi, Tunable magnetic properties in $SrRuO_3$/$BiFeO_3$ heterostructures via electric field. *J. Phys. Chem. C* **125**, 24052–24059 (2021).
24. Z. Y. Ren *et al.*, Nonvolatile ferroelectric field control of the anomalous hall effect in $BiFeO_3$/$SrRuO_3$ bilayer. *Phys. Rev. Appl.* **13**, 024044 (2020).
25. Q. Qin *et al.*, Emergence of topological hall effect in a $SrRuO_3$ single layer. *Adv. Mater.* **31**, 1807008 (2019).
26. J. He, A. Borisevich, S. V. Kalinin, S. J. Pennycook, S. T. Pantelides, Control of octahedral tilts and magnetic properties of perovskite oxide heterostructures by substrate symmetry. *Phys. Rev. Lett.* **105**, 227203 (2010).
27. W. Lu, P. Yang, W. D. Song, G. M. Chow, J. S. Chen, Control of oxygen octahedral rotations and physical properties in $SrRuO_3$ films. *Phys. Rev. B* **88**, 214115. (2013).
28. P. S. S. R. Krishnan *et al.*, Misfit strain driven cation inter-diffusion across an epitaxial multiferroic thin film interface. *J. Appl. Phys.* **115**, 054103 (2014).
29. L. Z. Li *et al.*, Giant resistive switching via control of ferroelectric charged domain walls. *Adv. Mater.* **28**, 6574–6580 (2016).
30. P. A. van Aken, B. Liebscher, Quantification of ferrous/ferric ratios in minerals: New evaluation schemes of Fe L-23 electron energy-loss near-edge spectra. *Phys. Chem. Miner.* **29**, 188–200 (2002).
31. P. S. S. R. Krishnan *et al.*, Mapping strain modulated electronic structure perturbations in mixed phase bismuth ferrite thin films. *J. Mater. Chem. C* **3**, 1835–1845 (2015).
32. Y.-M. Kim *et al.*, Direct observation of ferroelectric field effect and vacancy-controlled screening at the $BiFeO_3$/$La_xSr_{1-x}MnO_3$ interface. *Nat. Mater.* **13**, 1019–1025 (2014).
33. Y.-M. Kim *et al.*, Probing oxygen vacancy concentration and homogeneity in solid-oxide fuel-cell cathode materials on the subunit-cell level. *Nat. Mater.* **11**, 888–894 (2012).
34. I. Lazic, E. G. T. Bosch, S. Lazar, Phase contrast STEM for thin samples: Integrated differential phase contrast. *Ultramicroscopy* **160**, 265–280 (2016).
35. C.-L. Jia *et al.*, Atomic-scale study of electric dipoles near charged and uncharged domain walls in ferroelectric films. *Nat. Mater.* **7**, 57–61 (2008).
36. C. T. Nelson *et al.*, Spontaneous vortex nanodomain arrays at ferroelectric heterointerfaces. *Nano Lett.* **11**, 828–834 (2011).
37. L. Li *et al.*, Defect-induced hedgehog polarization states in multiferroics. *Phys. Rev. Lett.* **120**, 137602 (2018).
38. P. Gao *et al.*, Atomic mechanism of polarization-controlled surface reconstruction in ferroelectric thin films. *Nat. Commun.* **7**, 11318 (2016).
39. X. J. Li *et al.*, Atomic origin of spin-valve magnetoresistance at the SrRuO3 grain boundary. *Natl. Sci. Rev.* **7**, 755–762 (2020).
40. G. Cao, S. McCall, M. Shepard, J. E. Crow, R. P. Guertin, Thermal, magnetic, and transport properties of single-crystal $Sr_{1-x}Ca_xRuO_3$ (0<=x<=1.0). *Phys. Rev. B* **56**, 321–329 (1997).
41. L. Si, Z. Zhong, J. M. Tomczak, K. Held, Route to room-temperature ferromagnetic ultrathin $SrRuO_3$ films. *Phys. Rev. B* **92**, 041108 (2015).
42. W. L. Lu *et al.*, The role of octahedral tilting in the structural phase transition and magnetic anisotropy in $SrRuO_3$ thin film. *J. Appl. Phys.* **113**, 063901 (2013).
43. A. J. Grutter, F. J. Wong, E. Arenholz, A. Vailionis, Y. Suzuki, Evidence of high-spin Ru and universal magnetic anisotropy in $SrRuO_3$ thin films. *Phys. Rev. B* **85**, 134429 (2012).
44. S. R. Basu *et al.*, Phtotconductivity in $BiFeO_3$ thin films. *Appl. Phys. Lett.* **92**, 091905 (2008).
45. H. Matsuo, Y. Kitanaka, R. Inoue, Y. Noguch, M. Miyayama, Cooperative effect of oxygen-vacancy-rich layer and ferroelectric polarization on photovoltaic properties in $BiFeO_3$ thin film capacitors. *Appl. Phys. Lett.* **108**, 032901 (2016).
46. L. Pintilie *et al.*, Orientation-dependent potential barriers in case of epitaxial Pt-$BiFeO_3$-$SrRuO_3$ capacitors. *Appl. Phys. Lett.* **94**, 232902 (2009).
47. L. Wang *et al.*, Ferroelectrically tunable magnetic skyrmions in ultrathin oxide heterostructures. *Nat. Mater.* **17**, 1087–1094 (2018).
48. J. Matsuno *et al.*, Interface-driven topological Hall effect in $SrRuO_3$-$SrIrO_3$ bilayer. *Sci. Adv.* **2**, 1600304 (2016).
49. X. Yao *et al.*, Ferroelectric proximity effect and topological hall effect in $SrRuO_3$/$BiFeO_3$ multilayers. *ACS Appl. Mater. Interfaces* **14**, 6194–6202 (2022).
50. X. Li, Dislocation-tuned ferroelectricity and ferromagnetism of the BiFeO3/SrRuO3 interface. OSF. https://osf.io/qz5ak/. Deposited 9 March 2023.